Article

Xolography for linear volumetric 3D printing

https://doi.org/10.1038/s41586-020-3029-7

Received: 5 June 2020

Accepted: 2 November 2020

Published online: 23 December 2020

Check for updates

Martin Regehly[1]✉, Yves Garmshausen[2], Marcus Reuter[2], Niklas F. König[2], Eric Israel[3], Damien P. Kelly[2], Chun-Yu Chou[2], Klaas Koch[2], Baraa Asfari[1] & Stefan Hecht[4,5,6]✉

The range of applications for additive manufacturing is expanding quickly, including mass production of athletic footwear parts[1], dental ceramics[2] and aerospace components[3] as well as fabrication of microfluidics[4], medical devices[5], and artificial organs[6]. The light-induced additive manufacturing techniques[7] used are particularly successful owing to their high spatial and temporal control, but such techniques still share the common motifs of pointwise or layered generation, as do stereolithography[8], laser powder bed fusion[9], and continuous liquid interface production[10] and its successors[11,12]. Volumetric 3D printing[13–20] is the next step onward from sequential additive manufacturing methods. Here we introduce xolography, a dual colour technique using photoswitchable photoinitiators to induce local polymerization inside a confined monomer volume upon linear excitation by intersecting light beams of different wavelengths. We demonstrate this concept with a volumetric printer designed to generate three-dimensional objects with complex structural features as well as mechanical and optical functions. Compared to state-of-the-art volumetric printing methods, our technique has a resolution about ten times higher than computed axial lithography without feedback optimization, and a volume generation rate four to five orders of magnitude higher than two-photon photopolymerization. We expect this technology to transform rapid volumetric production for objects at the nanoscopic to macroscopic length scales.

We present a volumetric 3D printing process in which the structure of the entire resin volume is retained and complex multicomponent objects are manufactured and stabilized by the surrounding viscous fluid matrix. In contrast to sheet-based methods, support structures for overhanging features, requiring elaborate post-processing, are no longer required, layer-interface-associated anisotropies vanish and fragile, soft objects can be solidified. This method represents one-step fabrication of complete systems without requiring later assembly yet still incorporating moving parts.

Until now, two different light-based, volumetric technologies have received the most attention. To fabricate high-resolution microscale objects, two-photon photopolymerization is the state of the art and has realized objects with sub-100-nm feature sizes[16,17]. A major limitation is the volume generation rate, which is typically well below 1–20 $mm^3\ h^{-1}$ (refs. [18,19]), owing to the underlying nonlinear absorption process to harden a localized volume within the resin space. For volumetric additive manufacturing of macroscopic objects, computed axial lithography rotates a homogeneous resin volume while multiple images are projected into the target material at defined angles[14,20]. The superposition of expositions leads to a cumulated dose distribution of formed radicals, which solidify centimetre-sized objects within 30–120 s and leave other areas below the polymerization threshold. The technique requires a nonlinear response of the resin to define the threshold, which is at present mediated by an oxygen inhibition process. The resolution of printed objects has been reported as 300 µm, limited by dose fluctuations caused by light that passes through partially or already polymerized areas during the printing process. Recently, optimization and inclusion of a feedback system trying to compensate these effects during a second print of the same object resulted in 80-µm positive and 500-µm negative feature sizes[15].

In our approach, we eliminate the nonlinearities mentioned by using two intersecting light beams of different wavelengths to solidify localized regions. This approach, known as dual-colour photopolymerization (DCP), was proposed early on by Swainson[21]. Curing is mediated by a two-colour photoinitiator added to the resin, which is activated by a first wavelength, while absorption of the second wavelength either (1) initiates or (2) inhibits photopolymerization. The latter pathway frequently utilizes two-component photoinitiators and has been applied with success to two-colour photolithography[22,23], continuous layer-by-layer printing[12], and patterning of thin volumes[24]. Efficient route (1) photoinitiators required for deep-volume DCP are, however, not yet common. Molecular photoswitches[25] are valuable candidates[26], especially because each switching state can be precisely tailored with respect to its photochromic properties, absorption spectra, lifetime and chemical reactivity. Here, we leverage the potential of DCP to realize a true volumetric 3D printing technology by combining a novel dual-colour photoinitiator with a new projection light system for DCP, designed to achieve rapid, high-resolution printing.

Xolography

A light sheet of a first wavelength excites a thin layer of photoinitiator molecules from the initial dormant state to a latent state with a

[1]Technology Department, Brandenburg University of Applied Science, Brandenburg, Germany. [2]xolo GmbH, Berlin, Germany. [3]Institute of Materials Science, TU Dresden, Dresden, Germany. [4]Department of Chemistry and IRIS Adlershof, Humboldt-Universität zu Berlin, Berlin, Germany. [5]DWI—Leibniz Institute for Interactive Materials, Aachen, Germany. [6]Institute of Technical and Macromolecular Chemistry, RWTH Aachen University, Aachen, Germany. ✉e-mail: regehly@th-brandenburg.de; hecht@dwi.rwth-aachen.de

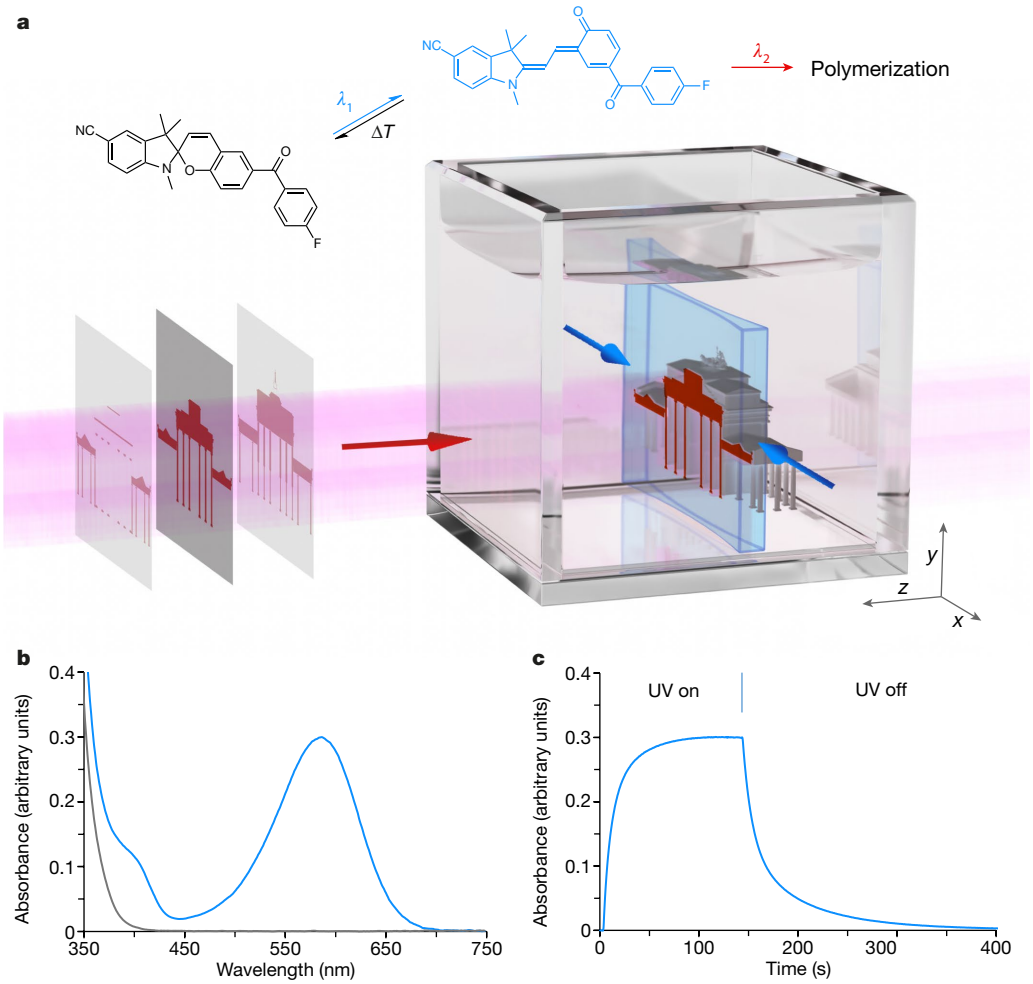

Fig. 1 | Xolography 3D printing technology. a, Rendered illustration of the printing zone and associated photoinduced reaction pathways of the DCPI. **b**, Absorbance spectrum of DCPI in resin 1 under dark conditions (grey) and 375 nm UV irradiation (blue). **c**, Photoswitching kinetics probed at 585 nm: generation of the DCPI active state during 375 nm UV irradiation at 1.5 mW cm^{-2} for 145 s, followed by thermal relaxation to the ground state in the dark.

finite lifetime (Fig. 1a). An orthogonally arranged projector generates light of a second wavelength and focuses sectional images of the three-dimensional (3D) model to be manufactured into the plane of the light sheet. Only the initiator molecules in the latent state absorb the light of the projector and cause the current layer to polymerize. By projecting a sequence of images during synchronized movement of the resin volume through the fixed optical setup, the desired object is continuously fabricated (Supplementary Video 1). The crossing (X) light beams generate the entire (holos) object using this printing process, hence the term xolography.

The dual-colour photoinitiator

Xolography requires a dual-colour photoinitiator (DCPI), which we realized by integrating a benzophenone type II photoinitiator into a spiropyran photoswitch. Although there have been a few reports on using the latter as photoswitchable precursors of radicals to initiate polymerization processes[27–29] our DCPI stands out by combining efficient photoswitching and photoinitiating properties with favourable spectral and thermal characteristics. The synthesis of the DCPI and related derivatives is straightforward and involves condensation of properly functionalized indole-based enamines with acylated salicylaldehydes (for synthetic details and characterization data see the Methods). The initial spiropyran state absorbs at the first wavelength (375 nm) and is completely transparent in the visible range of the spectrum. After switching to the latent merocyanine state, characterized by a broad transient absorption band covering the visible spectrum from 450 nm to 700 nm (Fig. 1b), absorption of the second wavelength generates the excited benzophenone moiety that, in combination with the co-initiator, initiates the radical polymerization process. Importantly, if the latent merocyanine is not hit with visible light, it reverts back to the initial spiropyran state with a thermal half-life of $t_{1/2} = 6$ s in the pentaerythritol tetraacrylate (PETA)-containing resin at room temperature (Fig. 1c). A potential drawback of the system arises from the fact that the merocyanine absorbs in the ultraviolet (UV) part of the spectrum as well, thereby opening up an unwanted competing initiation channel. The corresponding resins are optimized to provide high chemical reactivity for rapid polymerization and crosslinking, with maximum optical transparency as well as high viscosity.

The printer system

With the aim of suppressing the single-wavelength photoinitiation channel, we developed the light sheet approach to ensure that a voxel in the resin chamber is exposed to UV light only once. To generate the light sheet, a Gaussian beam of a 375-nm diode laser is transformed to a diverging laser line, further collimated and then focused into the centre of the print volume. The result is a beam waist that widens towards the edges of the vessel as depicted in Fig. 1a. Because of diffraction, the narrower the width in volume centre, the greater the widening at

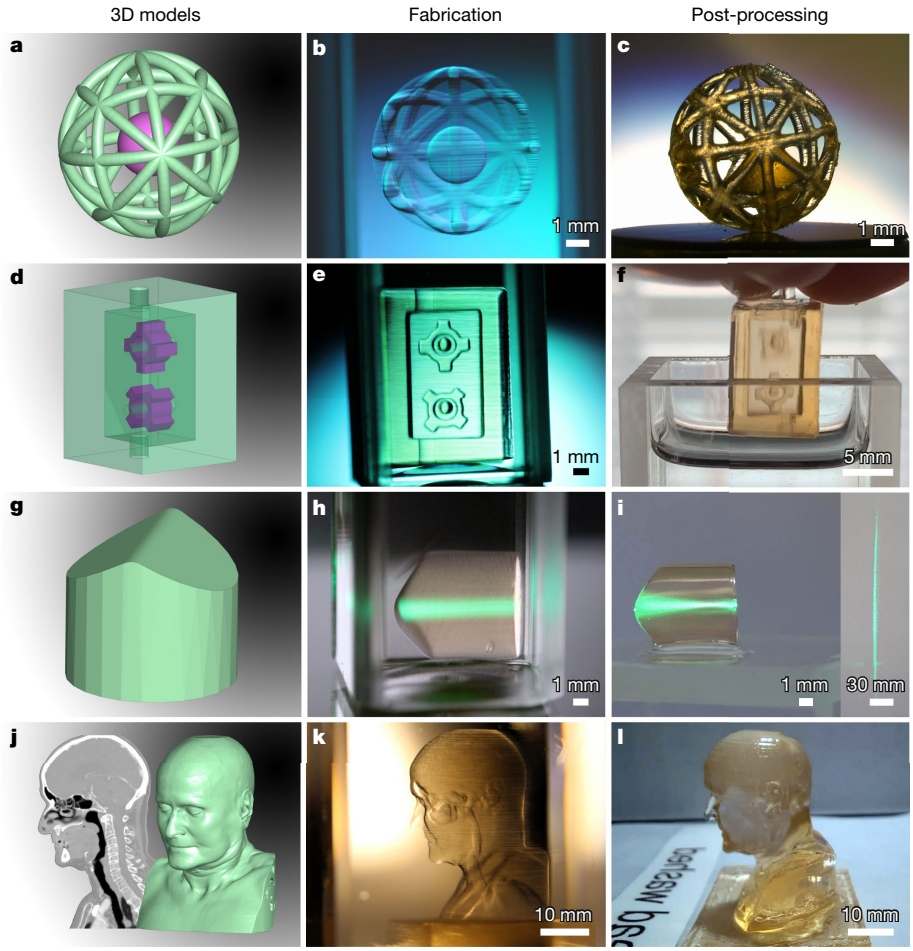

Fig. 2 | Volumetric digital manufacturing. 3D models (**a**, **d**, **g**, **j**) and photographs of printed objects before (**b**, **e**, **h**, **k**) and after (**c**, **f**, **i**, **l**) post-processing. **a**–**c**, Spherical cage with free-floating ball, 8 mm diameter. **d**–**f**, Encapsulated flow cell with rotary wheels, 9 mm in width. **g**–**i**, Aspherical Powell lens for laser line generation, 9 mm in width, as shown in the right inset. **j**–**l**, Anatomical model derived from the Manix CTA dataset, 30 mm in width.

the edges and vice versa. Since the width of the light sheet affects the print resolution in the *z* direction, we performed a theoretical analysis using Gaussian beam theory, as set out in the Methods, which shows that the optimum waist size scales with the square root of the volume depth. For the system studied and an accepted 10% beam expansion, optimal waist diameters are 34 µm, 59 µm and 108 µm full-width at half-maximum (FWHM) for volume depths of 1 cm, 3 cm and 10 cm. For printing in 10-cm-sized cuvettes, we realized a value of $d = 39$ µm FWHM light sheet waist size, as shown in Extended Data Fig. 5b, c.

Owing to absorption of photoinitiator molecules, the UV light is attenuated exponentially with increasing depth of penetration according to the Beer–Lambert–Bouguer law. This leads to inhomogeneous excitation and photopolymerization profiles along the light sheet. We compensate for this effect by dividing the light and irradiating the volume from both opposite sides. A theoretical analysis, as described in the Methods, indicates that by using such a superposition, for volume depths up to 10 cm, the excitation inhomogeneity along the light sheet can be kept below 13% for the typical photoinitiator concentrations employed.

For radiating slice videos into the light sheet, we use a digital light projector with 3,840 × 2,160 pixels (ultrahigh definition) and limit its output spectrum to the transient absorption bands of the activated photoinitiator molecules. The projection optics has been replaced to realize an image pixel size of 21 µm × 21 µm at the focus position in the light sheet plane. The irradiance of the projector was determined to be 215 mW cm^{-2}. It is more than one order of magnitude higher compared to the UV light sheet irradiance and thus favours the DCP pathway compared to competing single-wavelength initiation channels. A linear stage moves the resin vessel continuously away from the projector through the optical setup. In this way, the light rays only pass through transparent and homogeneous resin areas up to the target volume and are not disturbed by light refraction and scattering on completely or partially polymerized areas. The laser, linear axis and projector are controlled by a Python program running on a Raspberry PI 4 system.

Volumetric printing capabilities

The UV irradiance and speed of the vessel control fabrication for a specific resin composition. To determine the optimal values, we developed a calibration routine that tests several irradiance-speed pairs (Methods). As a result, a parameter space for xolography is obtained, which is limited by a minimum required UV light dose for two-colour curing and by a maximum dose above which undesired solidification by UV light alone occurs. For the PETA and diurethane dimethacrylate (UDMA)-based resins used here, we set a shift speed of 136.8 µm s^{-1} and a light sheet irradiance of 7 mW cm^{-2}. The UDMA monomer in resin 2 is more reactive, so the amount of co-initiator in this formulation could be reduced to below 1 wt%. Typical printing times are about one minute in 10 mm cuvettes, corresponding to a maximum volume generation rate of about 55 mm^3 s^{-1}. We first generated free-floating objects without any support structures, such as the ball in the cage (Fig. 2a).

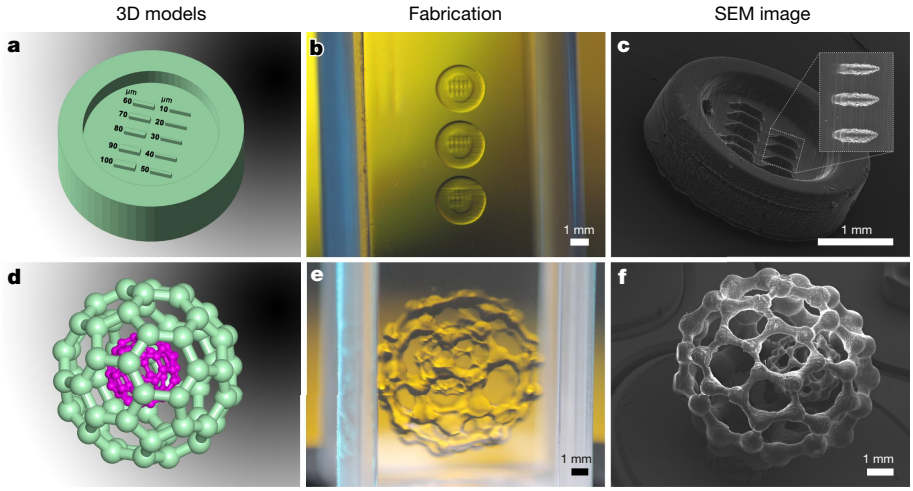

Fig. 3 | Characterization of high-resolution object features. 3D models (**a**, **d**), photographs of printed objects before post-processing (**b**, **e**) and SEM characterization after post-processing (**c**, **f**). **a**–**c**, Test plate of 3 mm diameter with bars of decreasing width down to 10 µm, as shown in the zoomed area on the top right. **d**–**f**, Nested fullerenes of outer diameter 8.5 mm, providing defined structures in various spatial directions.

The crosslinking of monomers leads to changes in density[15], which results in different sink rates of parts under gravity. The high printing speed and viscosity of the resin minimize this effect, so sinking only becomes apparent after fabrication has been completed, as seen in Fig. 2b. Finally, the ball can move freely within its housing because the structures remain well separated. This feature enables single-step fabrication of parts integrating mechanical functions; a simple example is the flow cell depicted in Fig. 2d–f. The wheels in the encapsulated cell quickly rotate in a liquid stream and react directly to changes in the flow rate (Supplementary Video 2). Except for fine lines along the light sheet associated to vertical (y) irradiance variations, all objects exhibit a homogeneous structure and smooth surface as a result of the fabrication process. This prompted us to print an aspherical Powell lens in a convenient orientation. After creation, the lens is still immersed in the resin, where the refractive index difference is too small to function properly (Fig. 2h). In air, however, the lens stretches a narrow green laser beam into a uniformly illuminated straight line using strong spherical aberration as depicted in Fig. 2i.

From these results, we went on to scale up the volume depth to 30 mm and focused on generation of complex positive and negative structures. From a computed tomography angiography dataset and subsequent reconstruction of the digital model, as set out in the Methods, a precise anatomical representation was produced (Fig. 2j–l). As with all other objects, we used the light brown colouration caused by photoproducts of the co-initiator to photograph the otherwise highly transparent results. The mechanical properties of the post-processed objects are comparable to materials fabricated by established additive manufacturing methods (Supplementary Video 3, Extended Data Fig. 9).

We proceeded to determine the resolution using two dedicated objects with defined structural sizes and orientations. First, we characterized a printed test plate of diameter 3 mm with bars of decreasing size (Fig. 3a–c) using scanning electron microscopy (SEM). The bar with the smallest width of 10 µm did not solidify because it is below the resolution of the projected image given above. For the prototype presented here, analysis of SEM images results in a resolution of approximately 25 µm in the x and y directions and 50 µm in the z direction. Finally, we printed a nested fullerene molecular model (Fig. 3d–f) with the smallest 'bond' diameter of 80 µm, which—after removal from the resin—still forms a mechanically stable structure with a diameter of 8 mm. The different orientation of the smallest structures enabled us to confirm that there are no outliers of resolution in certain spatial directions and, more importantly, that outer structures do not affect the printing accuracy in the interior volume.

Discussion and future perspectives

The volume generation rate as a measure of the printing speed is currently a factor of 10^4 to 10^5 higher than that of two-photon photopolymerization and of the same order of magnitude as that of computed axial lithography. It is already foreseeable that the speed will increase substantially using laser sources of the watt class (instead of 70 mW currently) and photoinitiators with faster thermal relaxation time. This further development brings us closer to an ideal volumetric method, characterized by a fast, quasi-spontaneous objectification. The size of the print volume is mainly limited in one coordinate (x) only, so large objects will be produced either in a stationary volume or in combination with continuous resin flow systems of unlimited size. By illuminating from several sides or rotating the light sheet of defined intensity distribution around the vessel, even deeper printing volumes are enabled yet require more complex setups. Similar to previously published approaches[7], 4D materials (where the fourth dimension is material complexity) could be realized by projecting greyscale and colour images that modulate the degree of crosslinking or activate different photoinitiators with distinct transient absorption bands. In the latter case, these could encode for different polymerization types that in combination with tailored organic, inorganic or cellular resins provide access to a wide variety of (bio)material systems.

Without any computer-aided optimization and feedback systems, the resolution is about ten times higher than all previously known macroscopic volumetric printing processes, and we see the potential to realize an accuracy of below 10 µm in the plane of the light sheet. Owing to the irradiation with two light beams of different wavelengths at a fixed angle, we are confident that the technology can be expanded to produce microscopic and nanoscopic objects using optical systems with a higher numerical aperture.

In summary, we present here a volumetric two-colour 3D printing technology, which is based on molecular photoswitches and does not require any nonlinear chemical or physical processes. The result is an enormously flexible approach that can be realized with readily available, cost-effective components. We expect that xolography will stimulate research fields from photoinitiator and material development to projection and light-sheet technologies, as well as having numerous applications that rely on rapid, high-resolution volumetric 3D printing.

Online content

Any methods, additional references, Nature Research reporting summaries, source data, extended data, supplementary information, acknowledgements, peer review information; details of author contributions and competing interests; and statements of data and code availability are available at https://doi.org/10.1038/s41586-020-3029-7.

1. Zastrow, M. 3D printing gets bigger, faster and stronger. *Nature* **578**, 20–23 (2020).
2. Galante, R., Figueiredo-Pina, C. G. & Serro, A. P. Additive manufacturing of ceramics for dental applications: a review. *Dent. Mater. J.* **35**, 825–846 (2019).
3. Najmon, J. C., Raeisi, S. & Tovar, A. Review of additive manufacturing technologies and applications in the aerospace industry. In *Additive Manufacturing for the Aerospace Industry* (eds Froes, F. & Boyer, R.) (Elsevier, 2019).
4. Ahmadi, A. et al. Additive manufacturing of laminar flow cells for single-molecule experiments. *Sci. Rep.* **9**, 16784 (2019).
5. Douroumis, D. 3D printing of pharmaceutical and medical applications: a new era. *Pharm. Res.* **36**, 42 (2019).
6. Lee, A. et al. 3D bioprinting of collagen to rebuild components of the human heart. *Science* **365**, 482–487 (2019).
7. Jung, K. et al. Designing with light: advanced 2D, 3D, and 4D materials. *Adv. Mater.* **32**, 1903850 (2020).
8. Hull, C. W. Apparatus for production of three-dimensional objects by stereolithography. US Patent 4,575,330 (1986).
9. Zhang, D. et al. Additive manufacturing of ultrafine-grained high-strength titanium alloys. *Nature* **576**, 91–95 (2019).
10. Tumbleston, J. et al. Additive manufacturing. Continuous liquid interface production of 3D objects. *Science* **347**, 1349–1352 (2015).
11. Walker, D. A., Hedrick, J. L. & Mirkin, C. A. Rapid, large-volume, thermally controlled 3D printing using a mobile liquid interface. *Science* **366**, 360–364 (2019).
12. de Beer, M. P. et al. Rapid, continuous additive manufacturing by volumetric polymerisation inhibition patterning. *Sci. Adv.* **5**, eaau8723 (2019).
13. Shusteff, M. et al. One-step volumetric additive manufacturing of complex polymer structures. *Sci. Adv.* **3**, eaao5496 (2017).
14. Kelly, B. E. et al. Volumetric additive manufacturing via tomographic reconstruction. *Science* **363**, 1075–1079 (2019).
15. Loterie, D., Delrot, P. & Moser, C. High-resolution volumetric additive manufacturing. *Nat. Commun.* **11**, 852 (2020).
16. Baldachini, T. *Three-Dimensional Microfabrication Using Two-Photon Polymerisation: Fundamentals, Technology and Applications* (Elsevier, 2019).
17. Zheng, L. et al. Nanofabrication of high-resolution periodic structures with a gap size below 100 nm by two-photon polymerisation. *Nanoscale Res. Lett.* **14**, 134 (2019).
18. Geng, Q., Wang, D. & Chen, P. Ultrafast multi-focus 3-D nano-fabrication based on two-photon polymerisation. *Nat. Commun.* **10**, 2179 (2019).
19. Saha, S. et al. Scalable submicrometer additive manufacturing. *Science* **366**, 105–109 (2019).
20. Bernal, P. N. et al. Volumetric bioprinting of complex living-tissue constructs within seconds. *Adv. Mater.* **31**, 1970302 (2019).
21. Swainson, W. K. Method, medium and apparatus for producing three-dimensional figure product. US patent US4041476A (1977).
22. Scott, T., Kowalski, B., Sullivan, A., Bowman, C. & Mcleod, R. Two-color single-photon photoinitiation and photoinhibition for subdiffraction photolithography. *Science* **324**, 913–917 (2009).
23. Liaros, N. & Fourkas, J. T. Ten years of two-color photolithography. *Opt. Mater. Express* **9**, 3006–3020 (2019).
24. van der Laan, H. L., Burns, M. A. & Scott, T. F. Volumetric photopolymerisation confinement through dual-wavelength photoinitiation and photoinhibition. *ACS Macro Lett.* **8**, 899–904 (2019).
25. Goulet-Hanssens, A., Eisenreich, F. & Hecht, S. Enlightening materials with photoswitches. *Adv. Mater.* **32**, 1905966 (2020).
26. Patel, S., Cao, J. & Lippert, A. A volumetric three-dimensional digital light photoactivatable dye display. *Nat. Commun.* **8**, 15239 (2017).
27. Jeudy, M. J. & Robillard, J. J. Spectral photosensitisation of a variable index material for recording phase holograms with high efficiency. *Opt. Commun.* **13**, 25–28 (1975).
28. Ichimura, K. & Sakuragi, M. A. Spiropyran-iodonium salt system as a two photon radical photoinitiator. *J. Polym. Sci. C* **26**, 185–189 (1988).
29. Lee, S.-K. & Neckers, D. Two-photon radical-photoinitiator system based on iodinated benzospiropyrans. *Chem. Mater.* **3**, 858–864 (1991).

Methods

Photoinitiator synthesis and characterization

The DCPI was synthesized in an overall three-step procedure involving initial syntheses of the 5-cyano-1,2,3,3-tetramethylindolenium and 4-fluoro-3′-formyl-4′-hydroxybenzophenone fragments, followed by their condensation as depicted in Extended Data Fig. 1.

5-Cyano-1,2,3,3-tetramethylindolenium iodide. 4-Cyanoaniline (5.9 g, 50 mmol) was dissolved in a mixture of concentrated aqueous hydrochloric acid (20 ml) and ice water (30 ml). Sodium nitrite (6.9 g, 100 mmol) in water (18 ml) was added at 0 °C. After stirring for 30 min, tin dichloride (28.4 g, 190 mmol) in concentrated aqueous hydrochloric acid (35 ml) was added. The resulting mixture was stirred for 30 min, filtered and washed with 1 M aqueous hydrochloric acid and water to obtain the hydrazine hydrochloride, which was used directly in the next step. The hydrazine hydrochloride salt (8.0 g, 47.5 mmol), 3-methylbutan-2-one (10.6 g, 86 mmol) and concentrated aqueous sulfuric acid (7 ml) were dissolved in glacial acetic acid (68 ml). The mixture was refluxed for 24 h and subsequently the main fraction of acetic acid was removed. After cooling to room temperature, the residue was neutralized with saturated aqueous sodium bicarbonate solution. The mixture was extracted with dichloromethane and the combined organic phases were dried over anhydrous magnesium sulphate, followed by evaporation of the solvent under reduced pressure to yield the crude indole. The obtained indole (5.5 g, 30 mmol) was dissolved in acetonitrile (150 ml), and methyl iodide (8.5 g, 60 mmol) was added . The mixture was refluxed for 24 h. After cooling to room temperature, the precipitated product was filtered and washed with acetonitrile. Recrystallization from acetonitrile yielded the product as a grey solid (6.8 g, 21 mmol, 42%).

4-Fluoro-3′-formyl-4′-hydroxybenzophenone. 4-Fluoro-4′-hydroxybenzophenone (8 g, 37 mmol) and sodium hydroxide (31 g, 780 mmol) were dissolved in water (160 ml) and heated to about 70 °C. Chloroform (6.0 g, 75 mmol) was added and heating was continued for 24 h. More chloroform (44 ml, 550 mmol) was added and heating was continued for another 24 h. After cooling to room temperature, the mixture was acidified with 10% aqueous hydrochloric acid and extracted with methyl *tert*-butyl ether. The combined organic layers were mixed with water (100 ml) and potassium hydroxide (7.5 g). The aqueous layer was washed with chloroform and then acidified with 10% aqueous hydrochloric acid. The aqueous phase was extracted with methyl *tert*-butyl ether and the combined organic extracts were dried over anhydrous magnesium sulphate. The solvent was removed under reduced pressure to yield the product as a white solid (1.5 g, 6.1 mmol, 17%). The product contains minor amounts of starting material, which are removed in the next step.

DCPI. 5-Cyano-1,2,3,3-tetramethylindolenium iodide (490 mg, 1.5 mmol) and piperidine (150 mg, 1.7 mmol) were dissolved in ethanol (5 ml) and stirred for 15 min. 4-Fluoro-3′-formyl-4′-hydroxybenzophenone (240 mg, 1 mmol) was added and the mixture was heated to 70 °C until consumption of starting materials as indicated by thin-layer chromatography. After cooling to room temperature, the product precipitated. The solid was filtered, washed with ethanol, and purified by recrystallization from ethanol to yield the product as white crystals (180 mg, 0.42 mmol, 42%).

^{1}H NMR (500 MHz, $CDCl_3$): δ (ppm) = 7.83–7.77 (m, 2H), 7.64–7.57 (m, 2H), 7.51 (dd, J = 8.2, 1.7 Hz, 1H), 7.29 (d, J = 1.6 Hz, 1H), 7.16 (t, J = 8.6 Hz, 2H), 6.96 (d, J = 10.3 Hz, 1H), 6.77 (d, J = 8.3 Hz, 1H), 6.54 (d, J = 8.2 Hz, 1H), 5.75 (d, J = 10.3 Hz, 1H), 2.82 (s, 3H), 1.32 (s, 3H), 1.19 (s, 3H). ^{13}C NMR (126 MHz, $CDCl_3$): δ (ppm) = 193.87, 166.28, 164.27, 157.77, 151.36, 137.50, 134.32, 134.29, 133.78, 133.02, 132.41, 132.34, 130.29, 129.85, 129.53, 125.36, 120.53, 119.22, 118.34, 115.65, 115.47, 114.95, 106.95, 105.07, 101.68, 51.87, 28.82, 25.87, 19.95. ^{19}F NMR (471 MHz, $CDCl_3$): δ (ppm) = −106.77. ESI-MS ($[M+H]^+$): m/z calculated for $C_{27}H_{22}FN_2O_2^+$: 425.166 measured: 425.172; see Extended Data Figs. 2–4 for nuclear magnetic resonance (NMR) spectra.

Resin composition and preparation

Resin 1: 19.0 g PETA were added to a solution of 2.4 mg (0.01 wt%) DCPI in 1.0 g (5 wt%) triethanolamine. Resin 2: 39.6 g UDMA were added to a solution of 4.8 mg (0.01 wt%) DCPI in 0.4 g (1 wt%) *N*-methyldiethanolamine. Resin 3: 38.8 g UDMA and 1.0 g 2-hydroxyethylmethacrylate were added to a solution of 2.4 mg (0.005 wt%) DCPI in 0.2 g (0.5 wt%) *N*-methyldiethanolamine. Resins were prepared by mechanically stirring a mixture of DCPI, co-initiator and the monomer(s) of choice in a 50-ml plastic tube followed by 10 min centrifugation at 4,000 rpm to remove residual air bubbles.

Irradiation measurements and UV/visible spectroscopy

A power and energy meter, model PM320C, and a Si photodiode power sensor, model SV120VC, from Thorlabs were used for irradiance measurements. UV/visible spectra and kinetic traces were recorded on a Cary 60 equipped with a thermostated cell holder at 25 °C in a 10 mm × 10 mm 3.5-ml quartz cuvette with four clear sides.

3D printer assembly

All components of the system are mounted on an optical table, a schematic representation is shown in Extended Data Fig. 5a. The beam of a 375 nm max. 70 mW continuous-wave diode laser (model IBEAM Smart, Toptica Photonics) is transformed to a diverging laser line by a Powell lens with 30° fan angle (Edmund Optics, part number 43-473) and further collimated by a cylindrical lens, f = 150 mm (Thorlabs, part number LJ1895L1-A). A second perpendicular oriented cylindrical lens, focal length depending on volume depth, focuses the light sheet in the centre of the cuvette. A UV beam splitter plate 50R/50T (Edmund Optics, part number 48-193) splits the beam into two arms. Two UV mirrors (Edmund Optics, part number 39-223) placed in each arm on opposite sides of the cuvette redirect the light to superimpose the light sheet in the printing volume. We characterized the properties of the light sheet in one arm by placing the focal plane of a digital camera (model EOS 1300D, Canon) with removed objective lens at the waist position of the light sheet. The image sensor has a pixel pitch of 4.29 µm. From a horizontal lineout, the diameter of the light sheet has been determined to 39 µm FWHM (Extended Data Fig. 5b, c). Videos are radiated using a digital light projector (model Acer GM832, 3500 ANSI Lumen). The projection optics has been replaced by a Braun Ultralit PL objective, f = 90 mm, f/2.4 and realizes an image plane size of approximately 80 mm (width) × 45 mm (height) in the light sheet plane. The projected pixel size of 21 µm × 21 µm is well above the diffraction limit of about 3.2 nm, determined by the objective's f-number of f/2.4 and assumed centre wavelength of λ = 550 nm using the Rayleigh criterion[30]. The light output is filtered using a UV/infrared cut-off filter from Baader Planetarium (order number 2459206). A servo-driven linear stage (model M-505.4PD) and a Mercury C-862 II controller from Physik Instrumente is used to move the resin vessel, the resolution is 0.25 µm at a minimum increment of 0.25 µm per step. The laser, linear axis and projector are controlled over two RS232 and one HDMI interfaces of a Raspberry PI 4 model B that is operated by a Python program running under a Raspbian operating system.

Data preprocessing, printing and post-processing

3D computer-aided design (CAD) models of the ball in the cage and the fullerene were downloaded from Thingiverse.com, Makerbot Industries, NY. Laserline Optics Canada Inc., BC, supplied the CAD model of the Powell lens whereas the flowcell and resolution test targets are self-designed with Tinkercad, Autodesk. The Manix CTA dataset originates from ref. [31], the associated 3D model was reconstructed using 3DSlicer[32] and the resulting mesh was cleaned using Meshmixer, Autodesk. Slice images were generated from 3D models using ChiTuBox, CBD-Tech, SZX and Hyperganic software, MUC; the resolution has been set to r = 3.8 µm per slice. Davinci Resolve, Blackmagic

Design, VIC, served to assemble slice images into ultrahigh-definition black-and-white printing movies. Objects were printed by executing a Python script, which starts the axis movement at a defined speed v and laser irradiation, followed by the playback of the print movie at a frame rate specified by v/r. Post-processing was carried out by removing the printed objects from the resin and washing them in isopropyl alcohol. Subsequently, we cured the objects for 5 min using a 375 nm UV light-emitting diode (model SM2F32-A from Thorlabs) at an irradiance of approximately 20 mW cm^{-2} and finally heated the objects for 40 min at 70 °C under air.

Calibration procedure for volumetric printing

An automated protocol was developed to find optimized printing parameters for a specific resin composition by variation of UV light sheet irradiance E and printing velocity v. For this purpose, the video source projected a still image of a white rectangle into the resin volume as the cuvette was moved continuously through the printing zone at discrete speeds. The UV light sheet was turned on for a given velocity until a 500-µm block was irradiated, followed by an empty separation distance of 500 µm (Extended Data Fig. 6b). The same procedure was repeated for different light sheet irradiances to obtain a matrix of results. An optical readout detected whether an irradiance velocity-combination led to unspecific material solidification, a sharp defined block or no solidification at all. Each dot in Extended Data Fig. 6 represents a classified result. In case of unspecific solidification (purple dots), the competing single-wavelength activation channels of the photoinitiator molecules lead to UV-light-induced curing; see section 'The dual-colour photoinitiator' for details of this mechanism. At higher speeds, the UV radiation dose per volume decreases, and solidification then only takes place in combination with additional irradiation from the projector (green dots). This is the desired parameter space of dual-colour photopolymerization on which xolography is based. No solidification is observed (even for the projector turned on) when the UV dose is too low (grey dots). In this case, the concentration of activated photoinitiator molecules is too low to provide sufficient crosslinking between monomers via the initiated radical polymerization.

The parameter space for xolography is a triangle in the diagram of Extended Data Fig. 6. For a particular resin composition, the minimum UV dose required to harden a cubic volume of 1 cm^3 is given by the slope $\Delta E/\Delta v$ of the dotted line separating the xolography from the no-solidification area. For resin 1, the required UV light dose is about 0.3 J cm^{-3}. This value enables an estimate of the minimum necessary printing time for a certain volume size.

Scanning electron microscopy and mechanical characterization

A JEOL JSM-6490 LV scanning electron microscope was used to acquire topographic images of the printed samples by detection of the secondary electrons. The electron beam energy was 20 keV; the magnification was between 10× and 35×. Before the measurement, samples were coated with a thin layer of gold of approximately 35 nm using a Bal-Tec SCD 050 sputter coater.

The mechanical properties of a post-processed object printed using resin 3 were qualitatively tested by simple resistance to shock (Supplementary Video 3). Quantitatively, the ultimate tensile strength of the printed test specimen (l_0 = 40.2 mm, b = 4.7 mm, w = 7.7 mm) was determined to be R_m = 51.4 MPa by tensile testing (Extended Data Fig. 9a) using a Zwick Roell Z020 TN. Additionally three-point flexural testing (Extended Data Fig. 9b) was performed using a Netzsch DMA 242 (specimen dimensions: l = 40 mm, b = 6.5 mm, w = 3.5 mm) yielding a storage modulus of E' = 2.6 GPa (20 °C).

Estimate of the optimal light sheet waist size depending on volume depth

The width of the light sheet limits the theoretical printing resolution in the z direction (that is, the direction of movement). The following model calculations were performed for resin 1 as an example. The contained PETA monomer (95 wt%) controls the dispersion properties of the resin to a good approximation. Two values of its refractive index were taken from the literature[33,34]: n = 1.478 (656 nm) and n = 1.487 (589 nm). The reduced Cauchy transmission equation[35] $n(\lambda) = A + \frac{B}{\lambda^2}$ represents an empirical relationship between n and the wavelength of light for a transparent material in the normal dispersion regime. Using the two reference numbers, the coefficients A and B were determined to be 1.44 and 16823.71, respectively; the value of the refractive index of resin 1 at 375 nm is therefore about 1.56.

The horizontal intensity distribution of the light sheet is similar to a Gaussian function, so it is adequate to model the evolving beam width of the light sheet using Gaussian beam theory[30]. The 1/e^2 half-diameter of the light sheet for a distance x from focus is given by: $w(x) = w_0\sqrt{[1 + (x/x_R)^2]}$. At a distance equal to the Rayleigh range x_R, the half-diameter w of the beam is $\sqrt{2}$ larger than it is at the focus where $w = w_0$, the beam waist. Both parameters x_R, as a measure for beam divergence, and w_0, characterizing the smallest possible beam width, depend on each other and are influenced by wavelength λ according to: $w_0 = \sqrt{\lambda\, x_R/\pi}$ and $x_R = \pi w_0^2 n/\lambda$. We are seeking a compromise between waist size at focus and beam width at the vessel windows expressed by a homogeneity factor β, which specifies the acceptable width increase. In the case of β = 1.1, we tolerate a 10% deviation from centre to window distance $\Delta = D/2$, where D is the volume depth. By setting $w(\Delta) = \beta w_0$ and using the above-mentioned equations, we can solve for the waist size, which yields $w_0 = \sqrt{\lambda/\pi n(\Delta/\sqrt{\beta^2 - 1})}$. It is more obvious to approximate the polymerization threshold by the FWHM of the light sheet rather than the half-diameter w_0 at 1/e^2, the relationship is given by: $d_{FWHM} = \sqrt{2\ln 2}\, w_0$. Extended Data Fig. 7 depicts the optimal FWHM waist sizes in dependency of volume depth D and for different beam widening factors β = 1.1, 1.2, 1.5, corresponding to 10%, 20% and 50% beam diameter increase. In the case of 10%, the optimal waist diameters are 34 µm, 59 µm and 108 µm FWHM for volume depths of 1 cm, 3 cm and 10 cm, respectively.

Light sheet superposition for homogeneous photopolymerization profiles

By passing through the resin, the 375 nm UV light sheet is attenuated by absorption and scattering along the propagation direction. By superimposing two light sheets that enter the resin vessel from opposite sides, we reduce this effect and obtain a more homogeneous excitation profile along the optical axis. Quantitatively, the intensity decreases from volume entrance with depth coordinate x according to the Lambert–Beer–Bouguer law: $I(x) = I_0 e^{-(\alpha_A + \alpha_S)x}$ whereas α_A and α_S denote the absorption and scattering coefficients, respectively. At 375 nm, absorption is caused by the photoinitiator, whereas monomer and co-initiator molecules do not contribute. During excitation, a fraction of photoinitiator molecules switches to the active state, thereby changing the absorption spectrum. This effect can be controlled by varying irradiance, optimization of the photoinitiator and changing the excitation wavelength, so we operate with the ground-state absorption properties of the photoinitiator. Typical photoinitiator concentrations used for xolography are between 0.3 mM and 0.9 mM, resulting in absorption coefficients of α_A = 0.1–0.3 cm^{-1} and corresponding optical densities of OD^{1cm} = 0.1–0.3 at 375 nm in 1-cm-sized cuvettes.

The influence of light scattering, expressed by the scattering coefficient α_S, is attributed only to the monomer in the resin, owing to the low concentrations of photoinitiator and co-initiator. To choose the correct elastic scattering model, we first determine the approximate diameter d of the monomer molecules. With the density ρ = 1.19 g ml^{-1} and molar mass M = 352.34 g mol^{-1} of PETA as an example monomer, we estimate the molecular volume by $V_m = M/(\rho N_A)$, where N_A is the Avogadro constant. We calculate d by assuming that the monomer

molecule has a spherical shape from $V_m = (4/3)\pi(d/2)^3$. The approximate size of the monomer molecules is about $d = 0.5$ nm, which is much smaller than 1/10 of the design wavelength ($\lambda = 375$ nm). In this case, Rayleigh light scattering is the dominant underlying process. For organic liquids we can estimate the scattering coefficient α_S from the Einstein-Smoluchowski–Cabannes formula[36,37]: $\alpha_S = \frac{8\pi^3}{3\lambda^4}\left[\frac{(n^2-1)(2n^2+0.8n)}{n^2+0.8n+1}\right]^2 k_B T \kappa_T \frac{6+3\delta}{6-7\delta}$. The refractive index of PETA at 375 nm has been determined above to be $n_i = 1.56$. k_B is the Boltzmann constant, and the resin is at room temperature $T = 293$ K. The isothermal compressibility is estimated to be $\kappa_T = 5.7 \times 10^{-10}$ Pa^{-1} based on literature values[38–40] for similar esters of pentaerythritol. For isotropic liquids the depolarization ratio δ is zero but it is known that many organic liquids have large depolarization ratios[4] of about 0.4. By using the latter value we obtain an upper estimate for the scattering coefficient of $\alpha_S = 7.6 \times 10^{-4}$ cm^{-1}, which is much lower than the absorption coefficient.

If we superimpose two beams of half-intensity in the volume of a resin vessel of diameter D by irradiating the vessel from opposite sides, the intensity is given by $I(x) = \frac{I_0}{2} \times \left[e^{-\left(\frac{OD^{1cm}}{1cm}+\alpha_S\right)x} + e^{-\left(\frac{OD^{1cm}}{1cm}+\alpha_S\right)(D-x)}\right]$.

Extended Data Fig. 8a, b shows the ratio I/I_0 along the depth axis for 1 cm volume depth for double-sided illumination and, for comparison purposes, also for single-sided irradiation. The superposition leads to a smooth redistribution. We quantify the maximum deviation from the peak-to-peak average intensity $I_{avg} = \frac{I(0)+I(D/2)}{2}$ by evaluating $\frac{\Delta I}{I_{avg}} = \frac{I(0)-I_{avg}}{I_{avg}} = \frac{I(0)-I(D/2)}{I(0)+I(D/2)}$. As depicted in Extended Data Fig. 8c, the intensity deviation increases with higher volume depths, leading to more inhomogeneous excitation profiles. For the employed photoinitiator concentrations (optical density of 0.15 at 375 nm) the concept of the superimposed light sheet is viable up to a volume depth of about 10 cm. In this case, the remaining inhomogeneity of about 15% from the average intensity I_{avg} for $OD^{1cm} = 0.1$ can be compensated by adjusting the projector intensity distribution. In particular, by multiplying the projector images with a grey value gradient, the degree of polymerization in the light sheet plane can be uniform despite the remaining inhomogeneous UV excitation.

Data availability

The data that support the findings of this study are available within the paper and Supplementary Information. Additional supporting data generated during the present study are available from the corresponding authors upon reasonable request.

30. Born, M. & Wolf, E. *Principles of Optics: Electromagnetic Theory of Propagation, Interference and Diffraction of Light* (Cambridge Univ. Press, 1999).
31. OSIRIX DICOM Image Library http://www.osirix-viewer.com/resources/dicom-image-library (accessed 2 April 2020).
32. Kikinis, R., Pieper, S. D. & Vosburgh, K. G. 3D Slicer: a platform for subject-specific image analysis, visualisation, and clinical support. In *Intraoperative Imaging and Image-Guided Therapy* (ed. Jolesz, F.) (Springer, 2014).
33. Aloui, F. et al. Refractive index evolution of various commercial acrylic resins during photopolymerisation. *Express Polym. Lett.* **12**, 966–971 (2018).
34. Liu, Y. et al. Improvement of the diffraction properties in holographic polymer dispersed liquid crystal Bragg gratings. *Opt. Commun.* **218**, 27–32 (2003).
35. Saleh, B. E. A. et al. *Fundamentals of Photonics* (John Wiley & Sons, 2019).
36. Zhou, X. et al. Rayleigh scattering of linear alkylbenzene in large liquid scintillator detectors. *Rev. Sci. Instrum.* **86**, 073310 (2015).
37. Coumou, D. J., Mackor, E. L. & Hijmans, J. Isotropic light-scattering in pure liquids. *Trans. Faraday Soc.* **60**, 1539 (1964).
38. Fandiño, O., Comuñas, M. J. P., Lugo, L., López, E. R. & Fernández, J. Density measurements under pressure for mixtures of pentaerythritol ester lubricants. Analysis of a density–viscosity relationship. *J. Chem. Eng. Data* **52**, 1429–1436 (2007).
39. Fandiño, O., Pensado, A. S., Lugo, L., Comuñas, M. J. P. & Fernández, J. Compressed liquid densities of squalane and pentaerythritol tetra(2-ethylhexanoate). *J. Chem. Eng. Data* **50**, 939–946 (2005).
40. Fandiño, O., Pensado, A. S., Lugo, L., Comuñas, M. J. P. & Fernández, J. Volumetric behaviour of the environmentally compatible lubricants pentaerythritol tetraheptanoate and pentaerythritol tetrananoanoate at high pressures. *Green Chem.* **7**, 775–783 (2005).

Acknowledgements We thank D. Radzinski for continuous support, F. Pinno and N. Wandel for SEM measurements, P. Fengler and A. F. Thünemann as well as J. Müller and A. Gurlo for help with material property measurements, S. Schneider and M. Dinter for 3D visualization of the printing zone, A. Steinbach for CAD modelling of the optical setup, and M. Vollmer for proofreading the manuscript.

Author contributions M. Regehly and S.H. designed the research and wrote the paper. Y.G. designed the spiropyran photoinitiator. Synthesis and characterization was performed by Y.G. and M. Reuter. Theoretical work and simulations by M. Regehly. Volumetric printer development was done by M. Regehly, M. Reuter, D.P.K. and C.-Y.C. 3D data processing was done by M. Reuter, E.I. and M. Regehly. Development of resin formulations, characterization and post-processing were performed by N.F.K., E.I. and Y.G. Software development was done by K.K. and B.A.

Competing interests Two patents (DE 10 2019 115 336 and DE 10 2019 129 868) have been filed related to the topic covered in this publication.

Additional information

Supplementary information is available for this paper at https://doi.org/10.1038/s41586-020-3029-7.

Correspondence and requests for materials should be addressed to M.R. or S.H.

Peer review information *Nature* thanks Cyrille Boyer, Robert McLeod and the other, anonymous, reviewer(s) for their contribution to the peer review of this work. Peer reviewer reports are available.

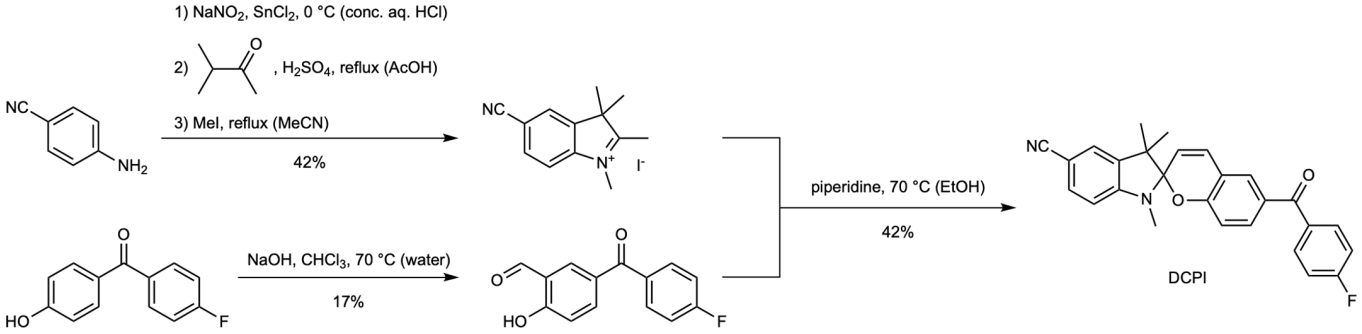

Extended Data Fig. 1 | Synthesis of DCPI. MeI, methyl iodide (CH_3I).

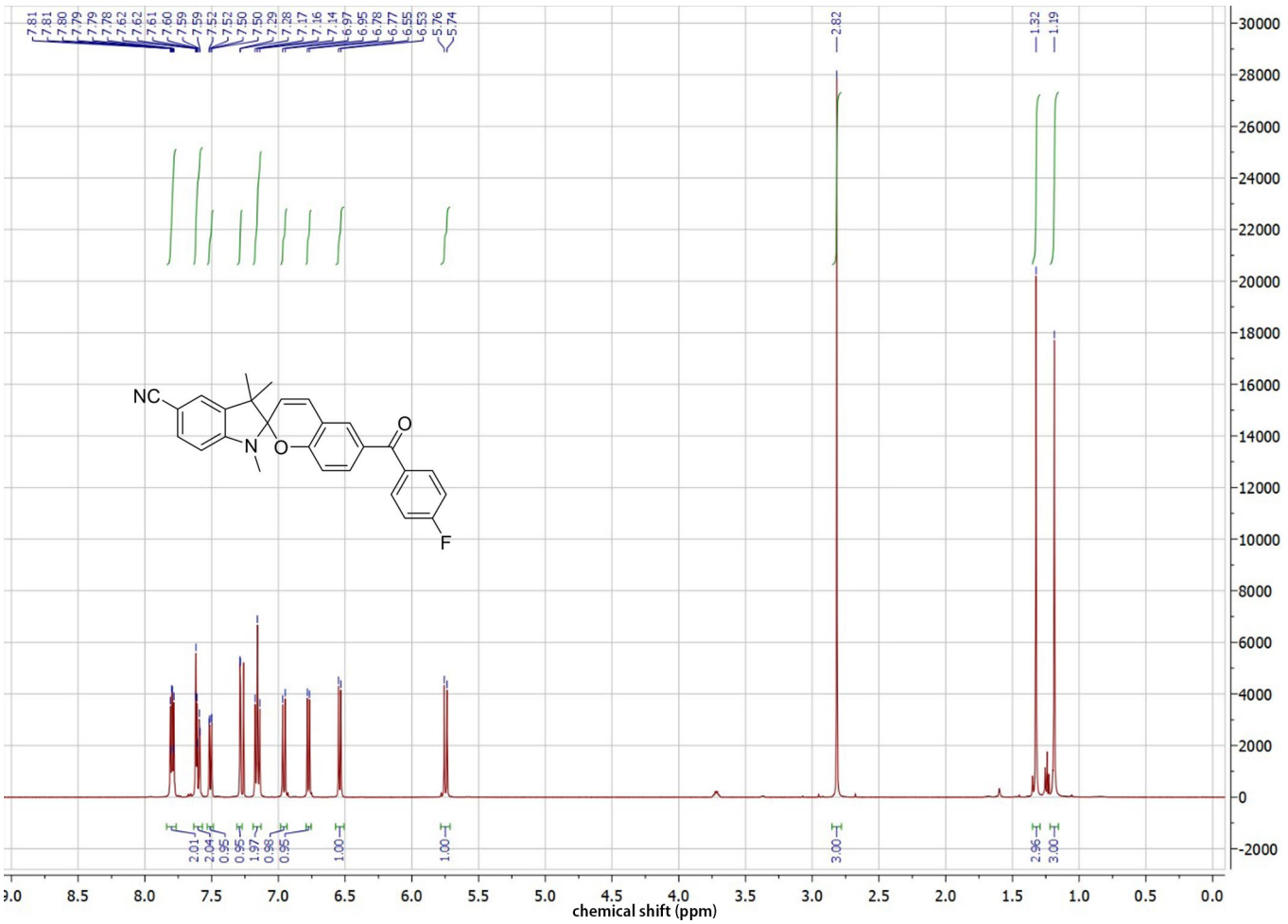

Extended Data Fig. 2 | ^{1}H NMR (500 MHz, $CDCl_3$) of DCPI.

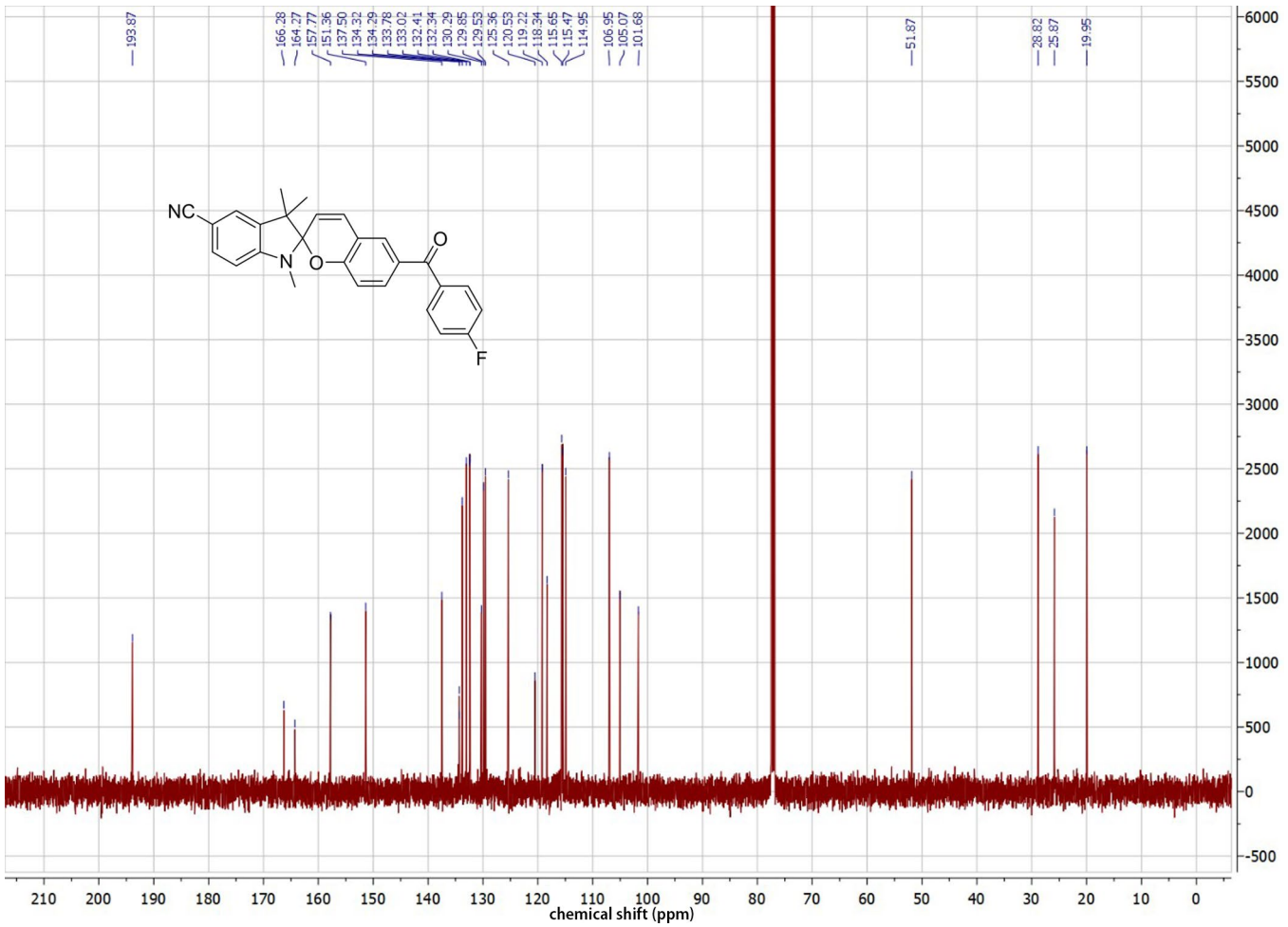

Extended Data Fig. 3 | ^{13}C NMR (126 MHz, $CDCl_3$) of DCPI.

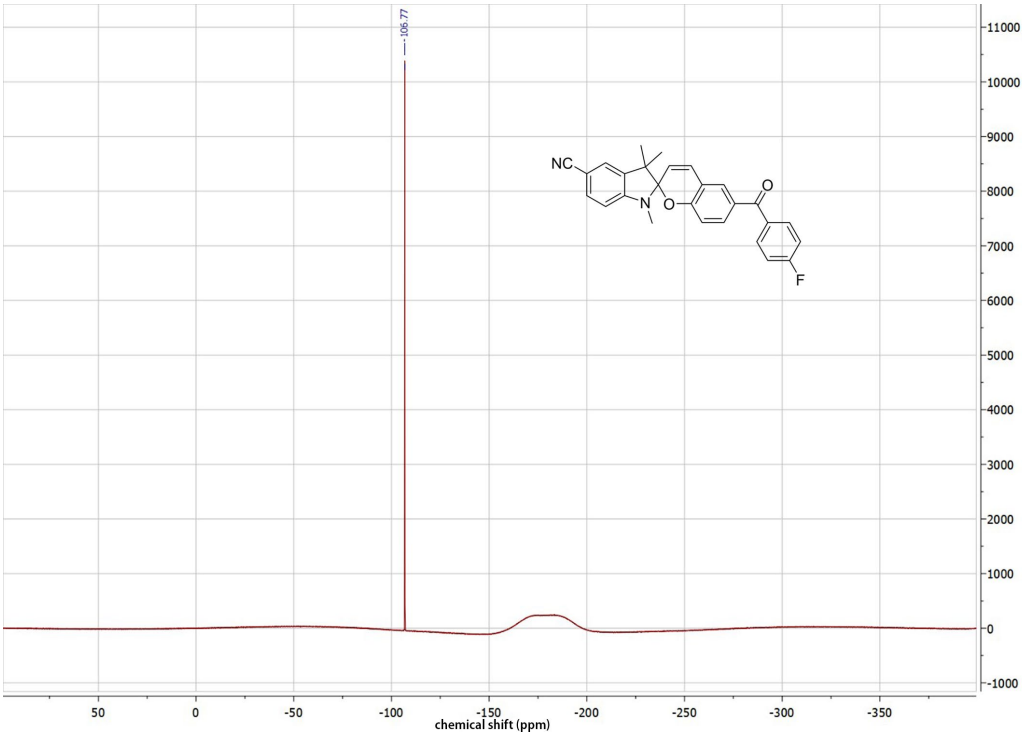

Extended Data Fig. 4 | ^{19}F NMR (471 MHz, $CDCl_3$) of DCPI.

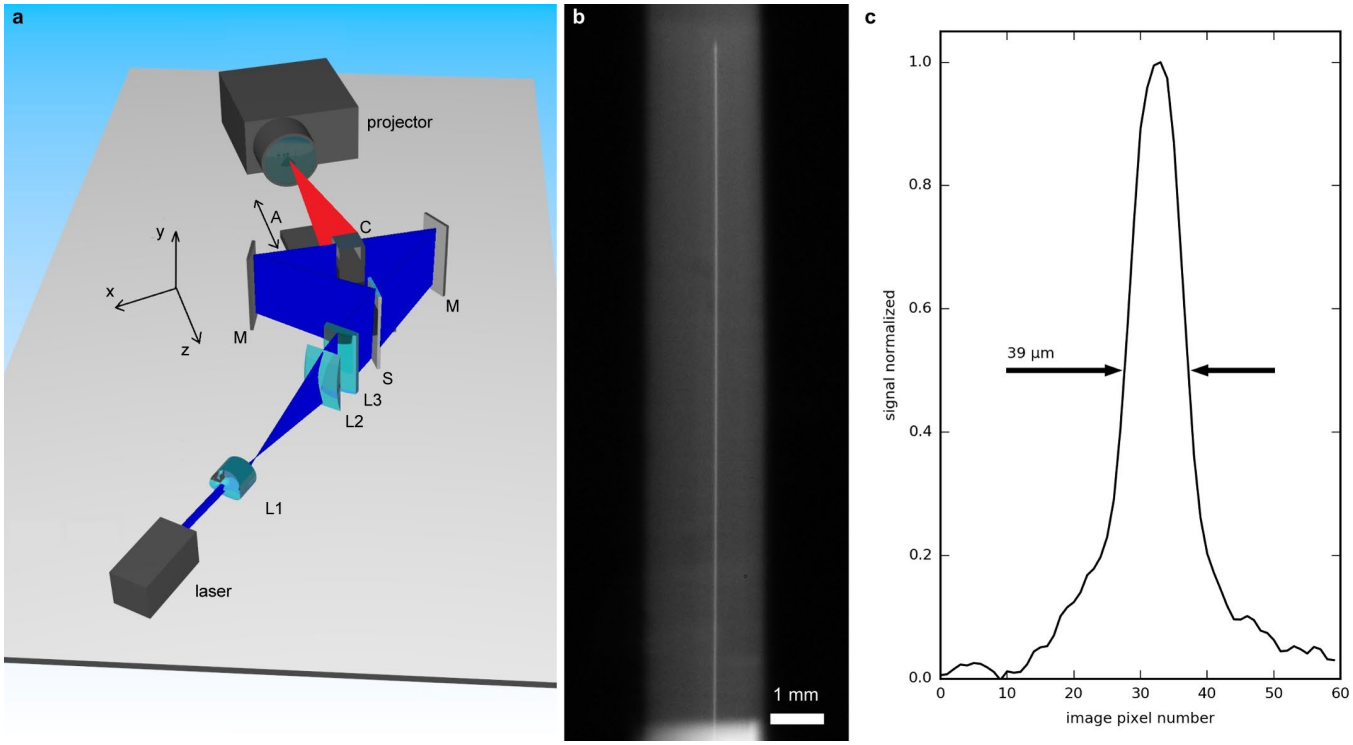

Extended Data Fig. 5 | Optical design and characterization of the light sheet generator. a, Schematic representation of the optical setup. L1, Powell lens. L2, L3, cylindrical lenses. S, beamsplitter. M, mirrors. A, linear axis. C, cuvette. **b**, Partial image of the light sheet in one arm at waist position. **c**, Horizontal lineout of the light sheet intensity distribution.

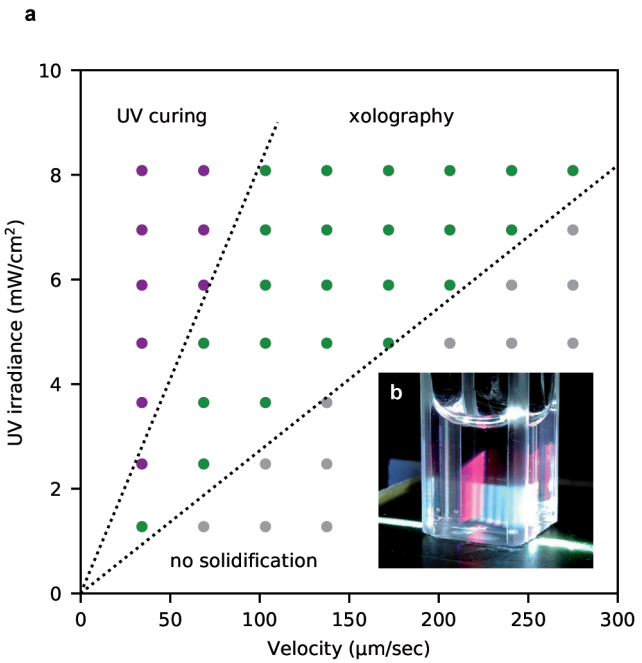

Extended Data Fig. 6 | Results of the calibration procedure. a, Diagram showing an array of tested irradiance/velocity combinations, which are used to identify the parameter space for xolography 3D printing. **b**, Photograph of the automated testing procedure in a 1-cm cuvette containing resin 1.

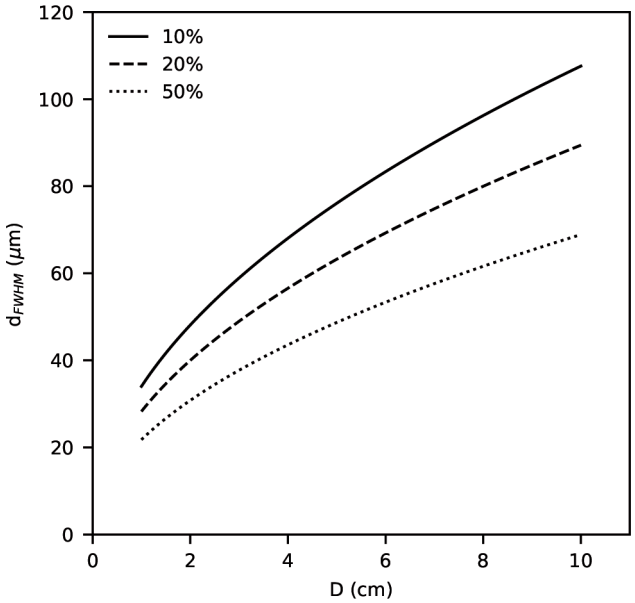

Extended Data Fig. 7 | Optimal light sheet waist widths. The plot shows the FWHM waist sizes d_{FWHM} of the light sheet against volume depth D for different values of the homogeneity factor β. The simulation has been performed for the design wavelength of $\lambda = 375$ nm and assumed refractive index of the resin of $n = 1.56$ (375 nm).

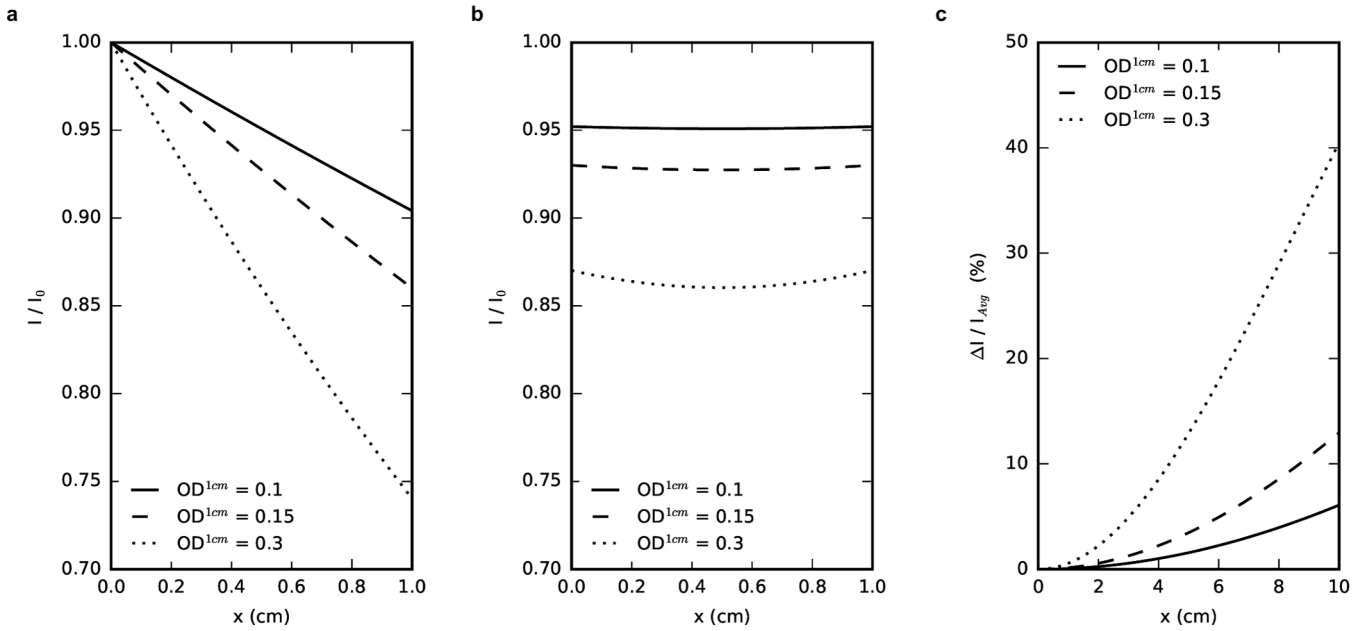

Extended Data Fig. 8 | Simulation of light sheet intensity distributions. **a**, Exponential intensity decrease along the 1-cm volume depth for single-side illumination. **b**, Double-sided illumination leads to a nearly homogenous distribution for 1-cm depth. **c**, Maximum deviation from the average intensity in percentage for volume depths of up to 10 cm.

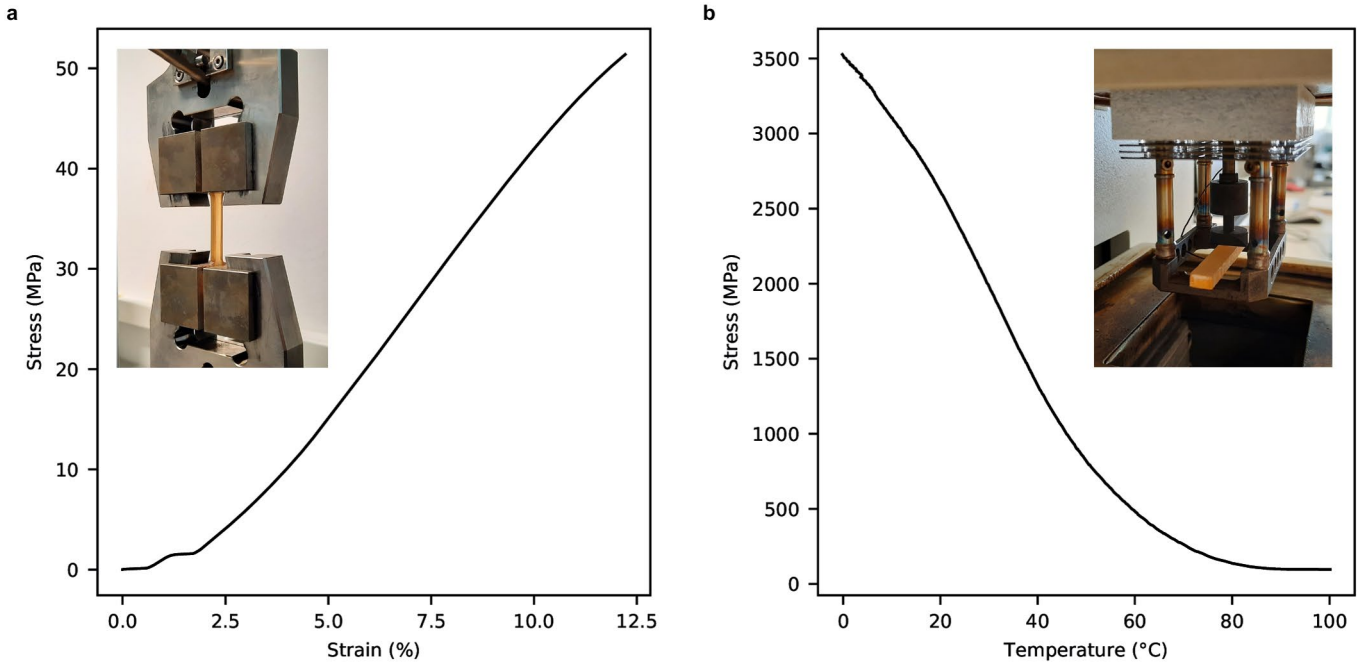

Extended Data Fig. 9 | Mechanical characterization of printed and post-processed test specimen. a, Stress–strain curve obtained at a nominal strain rate of $4 \times 10^{-2}\,s^{-1}$. The inset shows the sample mounted to the holder of the tensile testing machine. **b**, Modulus-temperature behaviour acquired using a 1 K min^{-1} heating ramp rate and an amplitude of 30 µm at an oscillation frequency of 1 Hz. The inset shows the sample mounted to the stage of the dynamic mechanical analyser.